Winter 12-14-2019

Enhanced Heat Transfer Performance by Shape Optimization of a Non-axisymmetric Droplet Evaporating on a Heated Micropillar

Haotian Wu
Washington University in St. Louis

Washington University in St. Louis

McKelvey School of Engineering

Department of Mechanical Engineering and Material Science

Thesis Examination Committee:

Damena Agonafer, Chair

David Peters

Ramesh Agarwal

Enhanced Heat Transfer Performance by Shape Optimization of a Non-axisymmetric Droplet Evaporating on a Heated Micropillar

By

Haotian Wu

A thesis presented to the McKelvey School of Engineering

of Washington University in St. Louis in partial fulfillment of

the requirements for the degree of

Master of Science

Dec 2019

St. Louis, Missouri

Dedication

I dedicate this thesis to my parents (Honghui Zhang and Xiaozhang Wu) and grandmother (Zesong Xiao) for nursing me with affections and love, and their life-time support and guidance.

Acknowledgments

First and foremost, I would like to express my deepest appreciation to my advisor Dr. Damena Agonafer whose continuous encouragement and invaluable guidance helped me a lot with coordinating my research especially in solving various issues during the research and setting up a goal for each step. I am also greatly grateful for what he taught me about the knowledge of heat transfer and thermal dynamics, and besides his passion, while he was teaching in the class and working in the lab, as the inspiration to make me constantly explore the science world.

Furthermore, I would like to acknowledge with much appreciation the crucial roles of my lab's colleagues who invested their effort to help me with my thesis. A special thanks go to Junhui Li who gave me a lot of suggestions on conducting simulations and addressing many kinds of numerical issues. I am also grateful for his thorough instruction to my research, and endless help with my thesis preparation. Moreover, thanks to Shan Li for helping me complete the simulation validation by adding the experimental results. Thanks to Zhikai Yang and MunMun for providing much advice on organizing and improving my thesis. Finally, I would like to show my greatest gratitude to Google Inc for its constant support to my research.

I would also like to express my appreciation to the committee members, Dr. Peters, Dr. Agarwal, and Dr. Agonafer, for attending my thesis defense.

Table of Contents

List of Tables

List of Figures

Abstract

Enhanced Heat Transfer Performance by Shape Optimization of a Non-axisymmetric Droplet Evaporating on a Heated Micropillar

By

Haotian Wu

Department of Mechanical Engineering and Materials Science

Washington University in St. Louis, 2019

Research Advisor: Professor Damena Agonafer

The stacked multilayer 3D IC structure used in next generation high-powered electronics poses great challenges in dissipating their large heat flux, which causes extreme difficulties for traditional cooling technologies. In response, more advanced two-phase liquid cooling technologies, such as droplet evaporation, which utilizes the latent heat of vaporization to remove excessive heat, have been widely investigated. Compared to traditional single-phase cooling techniques, two-phase cooling based on droplet evaporation offers both high efficiency and an exceptionally high heat dissipation rate. Compared to a spherical droplet, a non-spherical droplet on a non-axisymmetric pillar, with its different perimeter-to-area ratio and meniscus curvature, exhibits very different interfacial mass transport features. In particular, the higher ratio of the perimeter length to the solid-liquid area provides a relatively larger thin film region and therefore a smaller thermal resistance, while the high local curvature facilitates a stronger local vapor diffusion rate. However, the optimal pillar shape is still uncertain. In this study, using the Particle Swarm Optimization algorithm, we develop a shape optimization tool for max non-axisymmetric droplet evaporation on a micropillar structure. The optimization tool integrates the algorithm calculation and

curve generation in Matlab, the droplet shape generation in Surface Evolver, the geometry evolution in Solidworks, and the evaporation simulation in COMSOL. The optimized micropillar shape shows a 9% improvement in the heat transfer coefficient for the same liquid-vapor interfacial area and the same substrate area. Comparative evaporation experiments using fabricated micropillar samples with a baseline triangular pillar shape, validate the simulation results, with a relative error of less than 9.7% in evaporation rate.

Chapter 1. Introduction

This chapter briefly presents the background of the integrated circuit and its rapid development which brings about a great challenge in effectively dissipating the generated heat. In order to solve this problem, a variety of cooling strategies have been applied in different situations, among which the Two-phase cooling based on droplet evaporation, due to its excellent performance in heat transfer and high efficiency, win the most of people's plaudits. Specifically, Changing the shape of the droplet is one of the most effective ways to enhance heat transfer. Therefore, I design a set of specific procedures incorporating the Particle Swarm Optimization algorithm, droplet and micropillar building, and computational simulations to search for optimal shape.

1.1 Background and Motivation

As the shrinking feature size of integrated circuits (ICs) continues to decrease and approach the limits of traditional micro/nano fabrication, the development of 3-Dimensional IC technologies becomes a potentially reliable way to extend Moore's law [1]. Benefiting from increased packing density in the vertical direction, ICs allow for the application of multiple cores, memory, and logic units [2]. The stacked multilayer 3D IC structure, however, presents great challenges in effectively dissipating the generated heat flux taxing the performance of conventional cooling technologies [3, 4]. Compared to a critical heat flux of 300W/cm^2 in 2007, high performance microprocessors currently generate 1 kW/cm^2 on a device level and 5 kW/cm^2 in local hot spots [5, 6]. Reliable performance of high-performance electronic

systems demands that we develop advanced cooling technologies for power dissipation [7].

1.2 Present Cooling Strategies

When traditional single-phase air/liquid cooling strategies are embedded within high-performance electronic devices, it becomes extremely difficult for satisfying their cooling requirements. Although a microchannel-based liquid cooling system can offer sufficient cooling abilities for a heat flux of 800W/cm^2 at a substrate temperature at 71 ℃, it is limited by the increasing pressure head when it is scaled down [8]. Cooling strategies based on phase change heat transfer, such as boiling and direct evaporation, have been explored. By taking advantage of the high latent heat associated with the liquid-vapor phase change, these strategies remove a high heat flux from a small area at the expense of a small flow rate. However, heat transfer by boiling involves the generation and transport of vapor bubbles, which must first overcome capillary and static pressures in order to grow in the liquid, and then be transported to the vapor domain by buoyancy or convection flow. Additionally, boiling requires the heat source to be superheated in a subcooled or saturated liquid where additional thermal resistance is introduced by the nucleate boiling process [9]. Compared to boiling, direct evaporation from a thin liquid film is a more promising, because it achieves a large heat transfer coefficient without encountering high energy barrier for phase change [10-12].

1.3 Physical Mechanism of Droplet Evaporation

The efficiency of heat transfer by direct evaporation is dictated by the thin liquid film region fraction of the total evaporating surface. Although the thin film liquid region

only occupies only a small proportion of the evaporating area, it accounts for most of the evaporative heat transfer [13]. Specifically, for a wicking structure with a characteristic length of 60 mm, 80% of the phase change occurs in the thin film region, which occupies 20% of the total meniscus area [11]. The typical thin film evaporating region is an extended meniscus along the apparent contact line at the liquid/solid interface [14]. Hence, to enhance the overall evaporative heat transfer, the perimeter length along the contact line can be increased by extending the perimeter-to-surface area ratio.

By dividing up the evaporating meniscus into smaller segments using micropillars [15], micro-cavities [16] and microchannel structures [17, 18], the perimeter-to-surface area ratio can be increased considerably. Because this technique is restricted by the precision of the fabrication process, there is always a limitation on the characteristic dimensions of the microstructures. An alternate method for increasing the perimeter-to-surface area ratio is to modify the shape of the wetted region of the evaporating meniscus. As Sáenz et al. demonstrated, under adiabatic conditions, an evaporating droplet supported by a triangular base yields an evaporation rate 17% higher than a droplet on a circular base. Following Sáenz's work, Shuai el at. revealed a direct relationship between the local curvature and the local evaporation rate of non-spherical droplets [19]. All these studies illustrate how the shape of the base substrate has a significant effect on the droplet evaporation behavior.

1.4 Applications of PSO Algorithm

The base substrate shapes of the non-spherical droplets studied are regular polygons, which may not provide the largest heat transport. Shape optimization has been well developed and widely applied in a variety of applications. However, shape

optimization is usually combined with a complex multi-physics problem, so the traditional optimization methods are inefficient and inaccurate. Therefore, evolutionary algorithms like genetic algorithms (GA), the ant colony algorithm, the immune algorithm, and the particle swarm optimization algorithm (PSO) have been used to further improve the solution of complex optimization problems in real applications [20, 21].

Particle swarm optimization was first introduced by Kennedy and Eberhard [22] as a method based on a simplified social model. A physical analogy might be a school of fish who are adapting to their environment. In this analogy, each fish makes use of its own memory, as well as knowledge gained by the school as a whole, to adapt efficiently to its environment. Compared with the benchmark evolutionary genetic algorithms (GA), particle swarm optimization more efficiently explores the search space, which makes it more appropriate for applications in complex problems [20]. Fourie and Groenwold applied PSO to optimize the shape of a torque arm and the size of truss structures [23]. Upali K. Wickramasinghe et al. used a reference point based on multiple objective particle swarm optimization algorithms to optimize low-speed airfoil shape designs [24]. Although the PSO has also proved to be useful in many engineering design applications, such as logic circuit design [9], control design [10–12], and power systems design [13–15], the shape optimization of PSO in more complex multiphysics fields, such as the micro-heat exchanger, has been little explored.

1.5 Scope of the Thesis

In this study, we developed shape optimization tools for non-axisymmetric droplet evaporation on a micropillar structure. The shape optimization method integrated

shape generation by Matlab, equilibrated droplet shape generation by Surface evolver, and evaporation simulation by COMSOL into an iteration loop. The shape generation is controlled by the PSO algorithm to update the geometries from new iterations based on the objective value (i.e. the heat transfer coefficient) obtained in the evaporation simulation by COMSOL. The optimized shape is output when the convergence criterion is reached after a number of iterations, signaling that the optimization process is completed. The optimized micropillar shape shows a 9% improvement in the heat transfer coefficient for the same liquid-vapor interfacial area and the same substrate area. These evaporation experiments were conducted using fabricated micropillar samples of a baseline triangular pillar shape and an optimized pillar shape, and they validated the simulation results with a relative error of less than 9.7% in the evaporation rate.

Chapter 2. Simulation Methodology

A multiphysics simulation model was developed using COMSOL to predict the evaporation rate of non-axisymmetric microdroplets confined by different micropillar shapes. The evaporation process was analyzed in a steady-state condition, where the droplet was a fixed shape and evaporated at a constant rate. In the liquid domain, the heat transport is attributed to both conduction and convection. The convection current originates from three sources: (1) the continuous inlet flow from the center pore of the micropillar, (2) the buoyancy flow induced by the temperature difference between the bottom and top part of the microdroplet, and (3) the Marangoni flow induced by the temperature difference along the liquid-vapor interface. The Péclet number (*Pe*), the Rayleigh number (*Ra*), and the Marangoni number (*Ma*) can be applied to estimate the strength of the convection effect from each of the three sources, respectively. In this study, the Péclet number and Rayleigh number were found to be sufficiently small to neglect. The theoretically calculated Marangoni number, however, was found to often overpredict the Marangoni strength in experiments by 100 times for water droplets [25, 26]. Moreover, other studies have shown that the effect of Marangoni flow on evaporation is negligible for droplets with volume larger than 1 nL [27, 28]. As a result, the convective heat transfer in the liquid domain can be neglected. Therefore, in the liquid and solid domains, the heat transfer process is governed by the heat conduction equation, given by

$$\nabla^2 T = 0, \tag{1}$$

where T is the continuous temperature function in both the liquid and solid domains. The constant heat flux boundary condition, $q = 5 \times 10^6\ W/m^2$, was assigned to the

base surface of the micropillar. The vapor concentration in the gas domain is solved by the the steady-state species transport equation:

$$-\vec{V} \cdot \nabla C_v + \nabla \cdot \left(D_{diff} \nabla C_v\right) = 0, \quad (2)$$

where $\vec{V}$ is the velocity in the gas domain, driven by Stefan flow and thermal buoyancy flow. A constant concentration boundary condition was assigned at the far-field. This concentration is equal to the concentration of vapor in air where the relative humidity and temperature are 25% and 300K, respectively. A no-penetration (i.e., zero diffusive flux) condition was assigned to the solid-vapor interfaces. The evaporative flux along the liquid-vapor interface was calculated using equation (3), and the total evaporation rate was calculated using equation (4):

$$J = \bar{M} \cdot \left(-D_{diff} \frac{\partial C_v}{\partial n} + \vec{v}_n C_v\right) \quad (3)$$

$$\dot{m} = \iint_s J \, ds, \quad (4)$$

where J is the evaporative flux, $\bar{M}$ is the molecular weight, D is the diffusion coefficient, and n is the interface normal.

At the liquid-vapor interface, a heat flux thermal boundary condition was imposed to satisfy energy conservation between conduction and evaporative transport:

$$k_l \left(\frac{\partial T}{\partial \vec{n}}\right)_{lv} = D h_{fg} \left(\frac{\partial c_v}{\partial \vec{n}}\right)_{lv}, \quad (5)$$

where k_l is the thermal conductivty of water, h_{fg} is the latent heat of vaporization, D is the air–vapor molecular diffusion coefficient, and $c_{v,}$ is the vapor concentration at the liquid-vapor interface. Since the droplet size was large, the liquid-vapor interfacial pressure was not affected by the curvature of the droplet [28]. Therefore, the concentration at the liquid-vapor interface was assumed to be equivalent to the saturation concentration, i.e.,

$$c_{v,lv} = c_{sat}(T_{lv}), \tag{6}$$

where c_{sat} is the saturated vapor concentration, which can be found from a thermodynamic table [29]. The temperature and velocity in the gas domain are solved by incorporating the following continuity, momentum, and energy equations in the simulation model:

$$\nabla \cdot (\rho \boldsymbol{v}) = 0 \tag{7}$$

$$\rho(\boldsymbol{v} \cdot \nabla)\boldsymbol{v} = \nabla \cdot \left[-\rho \mathbf{I} + \mu[\nabla \boldsymbol{v} + (\nabla \boldsymbol{v})^T] - \tfrac{2}{3}\mu(\nabla \cdot \boldsymbol{v})\mathbf{I}\right] + \rho \mathbf{g}, \text{ and} \tag{8}$$

$$\rho c_p \boldsymbol{v} \cdot \nabla T - \nabla \cdot (k \nabla T) = \rho c_p \frac{\partial T}{\partial t} \tag{9}$$

The liquid-vapor interfacial temperature solved inside the droplet is used as the boundary condition for solving the temperature in the gas domain. The velocity boundary condition at the liquid-vapor interface in the gas domain is given by

$$\vec{\boldsymbol{v}}_n = \frac{1}{C_{air}} \cdot D \frac{\partial C_{air}}{\partial n} = -\frac{1}{C_g - C_v} \cdot D \frac{\partial C_v}{\partial n}. \tag{10}$$

In the simulation, the thermal buoyancy flow is taken into consideration by setting the air density as a function of the local temperature found by solving the heat transfer model. The simulation setup is detailed in Table. 1. Fig. 1 shows the schematic representation of the boundary conditions used in the simulations. At the far field, the vapor concentration and temperature are assigned as the ambient condition (the relative humidity and temperature are 25% and 300K); a vapor concentration boundary condition is assigned at the liquid-vapor interface, which equals the local saturation concentration which is the function of the local temperature; a constant heat flux boundary condition is applied at the pillar bottom surface, which is $500 W/cm^2$; The boundary condition of variable heat flux is set at the liquid-vapor interface, which is given by

$$q = -m_v \cdot h_{fg} \quad (11)$$

where m_v is the evaporation rate, and h_{fg} is the latent heat of vaporization of water; and all other walls are assigned as no-penetration boundary conditions. The far-field shape of the vapor domain is a hemisphere, set as 50 times larger than the characteristic length of the microdroplet (~100 μm). The microdroplets' shapes were imported from Surface Evolver.

Table 1.

Simulation setup

Imput parameters	**Value**
Outer diameter, *D*	100 μm
Inner diameter, *d*	50 μm
Interfacial area, A_{lv}	1.39×10^{-8} m^2
Substrate area, A_{sl}	7.85×10^{-8} m^2
Operating pressure, p_{amb}	101325 Pa
Solution methods	**Setup**
Mesh type	Tetrahedral
Study type	Stationary
Solver	Segregated
Geometric Multigrid Solver	GMRES
Preconditioning	Left

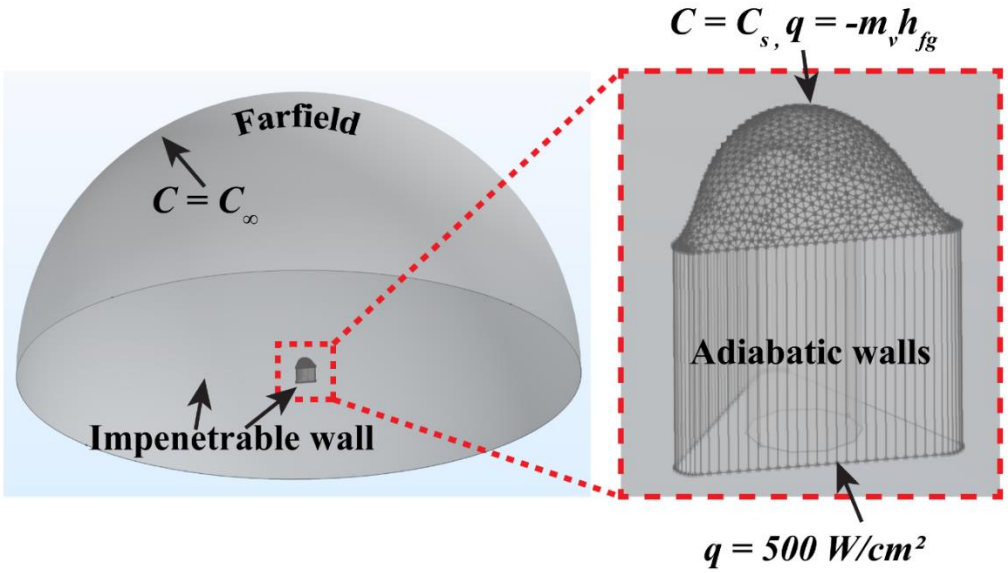

Figure 1. The boundary conditions for the numerical simulation of microdroplets evaporating on heated micropillars.

A mesh-independent study was conducted to investigate the influence of mesh size on the evaporation rate. As shown in Table 2, for triangular microdroplets, four levels of mesh with different element sizes (1.0 μm, 0.5 μm, 0.3 μm, and 0.2 μm) were generated for the mesh-independence study. The total evaporation rates for the coarse, medium, fine, and finest meshes were 1.15×10^{-10} kg/s, 1.17×10^{-10} kg/s, 1.18×10^{-10} kg/s, and 1.1985×10^{-10} kg/s, respectively. The difference in the rates for fine mesh and the finest mesh was only 1.5%. Therefore, the fine mesh with a element size of 0.3 μm was used for conducting the simulations.

Table 2.

Mesh independence study

Mesh size	Coarse	Medium	Fine	Finest
	1.06 million	1.38 million	2.58 million	4.05 million
Max element size on droplet surface (μm)	1.0	0.5	0.3	0.2

Evaporation rate (kg/s)	1.15×10^{-10}	1.17×10^{-10}	1.18×10^{-10}	1.19×10^{-10}
Variation with respect to 'Finest' mesh	3.7%	2.8%	1.5%	0%

Chapter 3. Optimization Methodology

3.1 Particle Swarm Optimization Algorithm

Based on the social behaviors of bird flocks and fish schools, which migrates to the most desirable regions, the particle swarm optimization algorithm (PSO) was developed for solving optimization problems. Different from the traditional genetic algorithm, PSO is well known for tracking the desired position of an object with a specified velocity by sharing the best solution (fitness) information. Benefitting from the communication between each candidate solution (particle) in PSO, the convergence rate of the algorithm is significantly improved over that of a traditional evolutional algorithm such as Genetic Algorithm.

The incorporation of the social behavior in the numerical process can be achieved by representing the population as a swarm and the individual as a particle. The position of a specific particle is updated incrementally according to its current position and velocity. The velocity is dependent on the position of the group-best particle and the desired position of the specific particle.

The general process of PSO can be demonstrated as follows:

1) Arrange the swarm to distribute the specified number of particles into random positions, and initialize them with random velocities and directions in a certain region.
2) For each particle, evaluate its fitness related to the problem which is being studied.
3) Compare the fitness of each particle with the fitness of the “particle-best” (pbest), which is the best value of its own. If the new value is better than the pbest, replace pbest with this new value.

4) Compare the fitness of each particle with the "group-best" (gbest), which is the best value of the overall group of particles. If the new value is better than the gbest, change the gbest to equal the new value, and modify the location of gbest to be the new location with the best fitness evaluation.

5) The new velocity vector of each particle for the next generation can be obtained by incorporating the position of the pbest and gbest into the memory of the whole swarm [30].

The following numerical equation illustrates how to get the new velocity for each particle:

$$v_{k+1}^{i} = wv_{k}^{i} + c_1 r_1 \left(p^{i} - x_{k}^{i}\right) + c_2 r_2 \left(p^{g} - x_{k}^{i}\right). \quad (12)$$

In (1) v_{k+1}^{i} is the velocity of the particle *i* at the *k+1* time iteration, and x_{k}^{i} is the current position of particle *i* at the *k*th time iterations. We take advantage of the p^{i} ,the position of the pbest, and the p^{g} , the position of the gbest, to adjust the path of the particles toward the desired region. Further, *w*, c_1, c_2 are three parameters that can be varied to improve the accuracy of the exploration and enhance the convergence rate. Finally, r_1 and r_2 are the random numbers between 0 and 1.

6) Update the positions for all particles based on equations (13) as follows:

$$x_{k+1}^{i} = x_{k}^{i} + v_{k+1}^{i}. \quad (13)$$

The new position for particle *i* at the *k+1* iteration is generated by incorporating the position at *k*th iteration and the velocity vector according to equation (12).

7) Repeat steps 2-6 until the desired fitness value is found and convergence is complete.

3.2 Overview of the Shape Optimization Method

For a micro-heat exchanger based on droplet evaporation and affected by the perimeter-to-area ratio of the pinned droplet, heat transfer performance is significantly related to the supporting micropillar's shape. The objective of this shape optimization research is to find the best micropillar shape, where the pinned droplet has the largest evaporative heat transfer performance. All the studied micropillar shapes have the same solid-liquid interfacial area (i.e., substrate area) A_{sl} = 7.85 × 10^{-8} m^2 and the same liquid-vapor interfacial area A_{lv} =1.39 × 10^{-8} m^2.

Figure 2 shows a general schematic of the shape optimization procedure. The four processes are (1) shape generation, (2) droplet and micropillar geometry generation, (3) evaporation simulation, and (4) optimization using the PSO Algorithm.

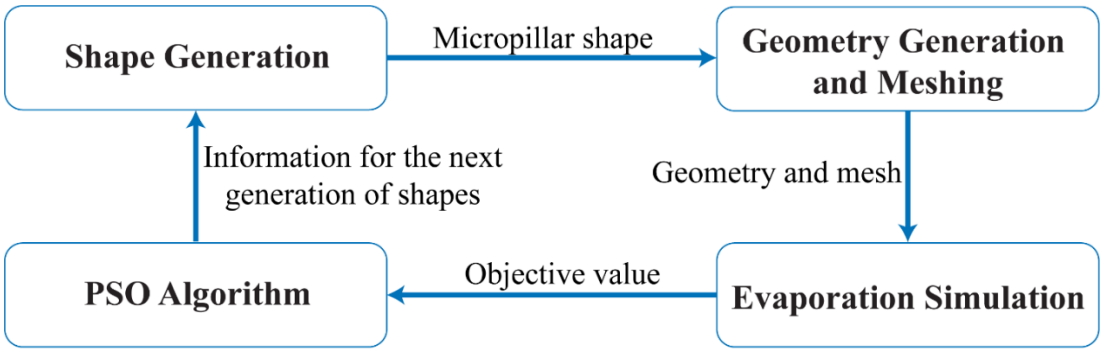

Figure 2. General schematic of information flow in the shape optimization process.

The micropillar shape is generated in Matlab and then imported into Surface Evolver and Solidworks to create droplet and micropillar geometries. The evaporation simulation is conducted in COMSOL, where the objective value (i.e., the heat transfer coefficient) of the particle is calculated. After importing the objective values of all the particles into the PSO algorithm, the next generation of micropillar shapes is

generated in Matlab. The shape optimization loop iterates for several generations until the final result achieves convergence and outputs the optimal micropillar shape [31].

3.3 Preliminary Simulations

The first step of shape optimization is to determine the baseline shape for the micropillar's geometry. The ultimate target shape will be a deformation of the baseline shape. However, it is difficult for the geometry optimization to begin with a random 2D shape. To develop the optimization tools without struggling with the deformation of a complex geometry, which increases the difficulties of convergence, we limited our initial choices to either a circular or normal polygon as the baseline case for this study. Then, because of the complexity of deforming either a circular shape or a complex polygon, we chose a triangle, the simplest possible polygon, as the baseline shape of the optimization, as shown in Figure 3(a). Further, so as not to introduce additional difficulties in simulations or fabrications of the micropillar, we chose a target geometry characterized by symmetric features. In addition, each edge of the target geometry is made up of a smooth curve with points at each ends Figure 3(b) provides several examples of the deformed triangular shapes, where a deformed equilateral triangle with convex or concave edges could be selected as our target shape.

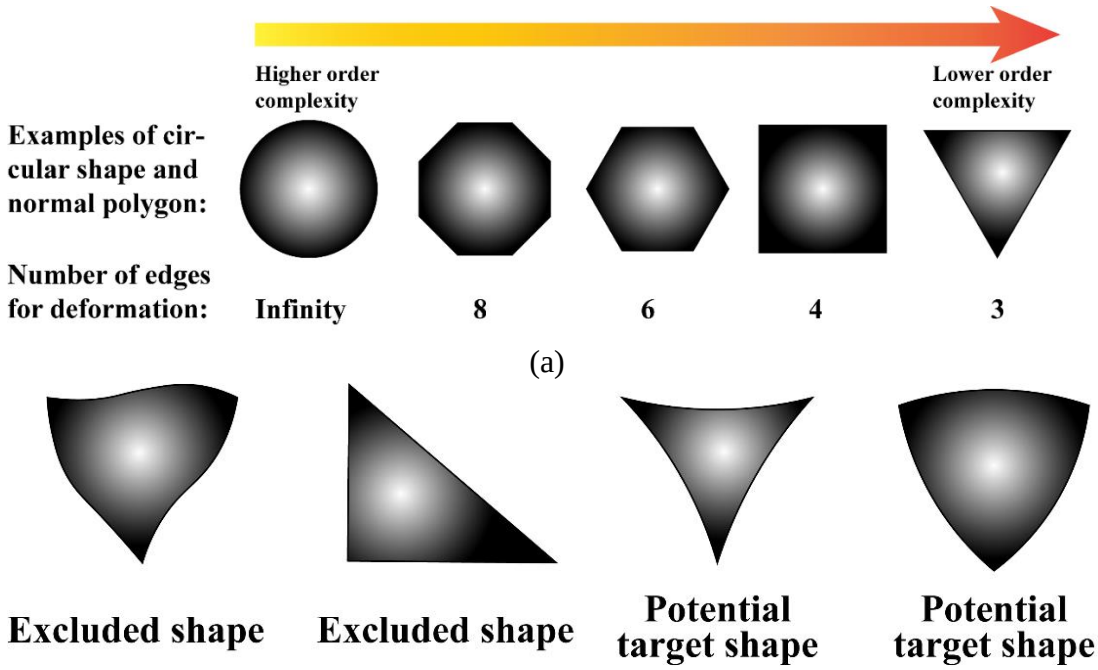

Figure 3. (a) Shape evolution of the baseline shape of micropillar geometry. (b) Examples of deformed triangular shapes.

Preliminary simulations were conducted for the general concave and convex deformed triangular shapes, following the simulation method introduced in section 2. Figure 4 illustrates the different thermal performances of three different triangle patterns. According to the preliminary tests, the micropillar with the concave pattern has a higher heat transfer coefficient than the equilateral pattern and convex pattern. Thus, the concave triangle was selected as the optimized target shape.

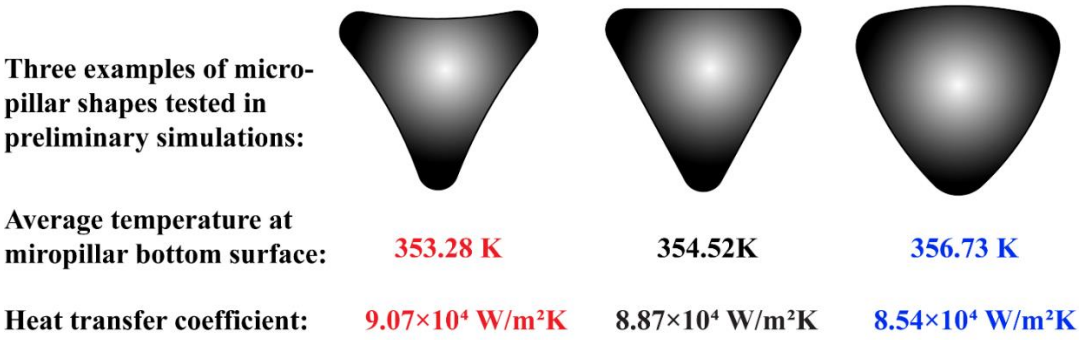

Figure 4. Heat transfer performance for three examples of triangular shape: concave, equilateral and convex

3.4 Micropillar Shape Parameterization

To parameterize a concave triangular pillar shape, a Bezier curve defined by numbers of control points is used to generate one edge of the triangle, and then to progressively form the micropillar shape. A Bezier curve is a parametric curve widely used in computer graphics and related fields [32]. This curve generation method is not only flexible and easy to manipulate but also yield a simple geometric control polygon, as well as a firm mathematical foundation [33].

In this research, the curve is defined by four control points, which is shown in Figure 5. P_1 and P_2 are two mirrored moving control points about the y axis, which gives the generated curve symmetry.

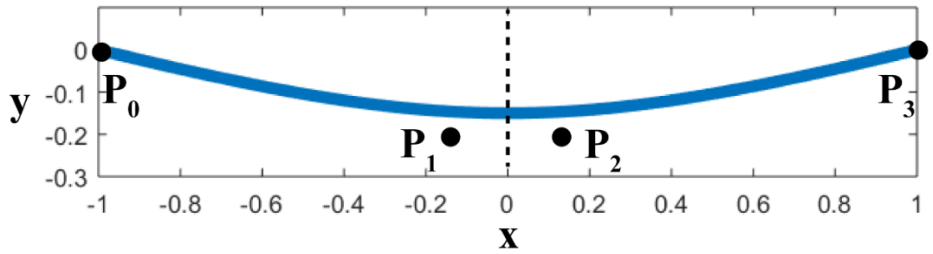

Figure 5. schematic diagram of a Bezier curve defined by four control points.

The positions of the moving control points are updated in every generation, and the micropillar shape is changed accordingly. The initial and terminal positions of the

curve are anchored by two fixed points P_0 and P_3. A Bezier curve is then defined by the four control points.

A Bezier curve satisfies the following formula, which can be defined for any degree of n:

$$B(t) = \sum_{i=0}^{n} \binom{n}{i} (1-t)^{n-i}\, t^i p_i, \qquad 0 \le t \le 1 \qquad (14)$$

where $\binom{n}{i}$ are the binomial coefficients, and p_i are the points on the curve. In this optimization study, the curve is defined by four control points, and Equation 14 can also be expressed as

$$B(t) = (1-t)^3 P_0 + 3t(1-t)^2 P_1 + 3t^2(1-t)P_2 + t^3 P_3, \qquad 0 \le t \le 1 \qquad (15)$$

Afterward, the integrated triangular shape is represented by rotating the curve by three times, as shown in Figure 6. The shape optimization problem is converted to determining the optimal coordinates of the control point.

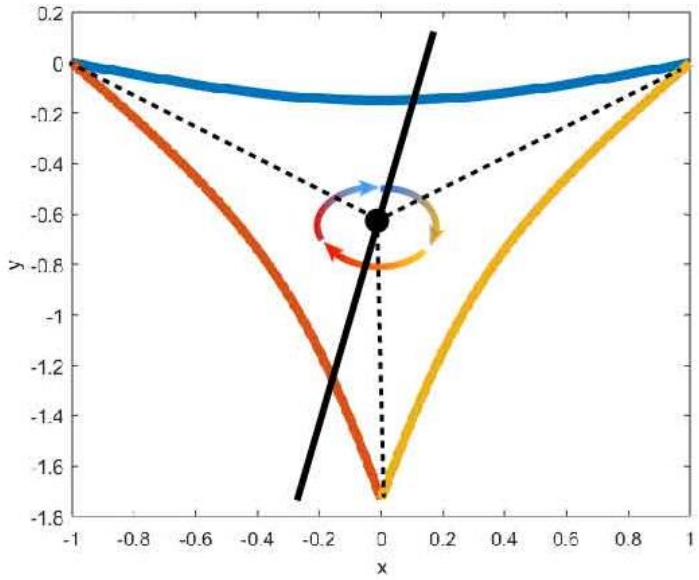

Figure 6. The symmetric micropillar shape generated by rotating a Bezier curve three times.

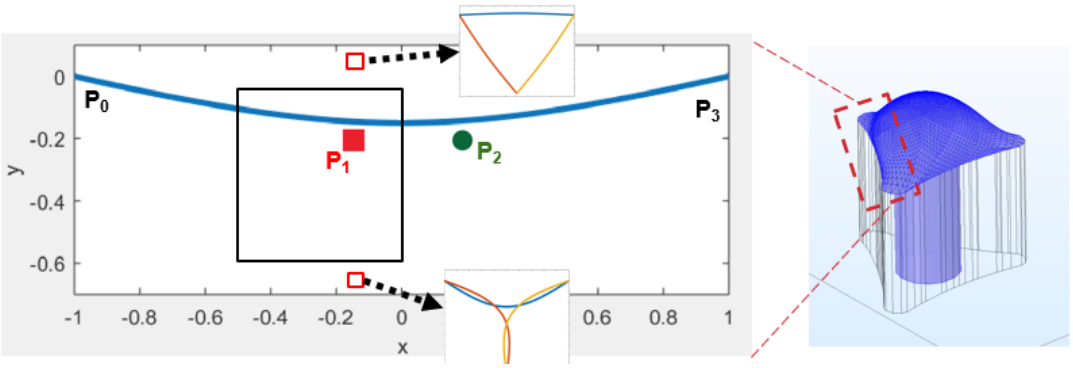

Figure 7. Schematic diagram showing two situations where the control point moves out of the restrictive box

The control point applied for each generation is constrained in a pre-defined region, as shown in Figure 7. In this box, the movement of the control point is limited to increase the convergence rate during the optimization process. As shown, the problem of two overlapped curves occurs as long as the control point drops below the box. If the control point moves above the box, the pillar shape becomes almost a regular equilateral triangular shape or a convex shape.

3.5 Implementation Details for PSO

3.5.1 Convergence Criterion

The convergence in the PSO is examined by comparing the objective function value for each particle at the specified number of iterations. If the difference in the function value between two consecutive iterations is less than 1%, the convergence is considered to be accomplished.

3.5.2 Initial Settings

The search space is assigned as a relatively small box, according to the results from preliminary simulations, which significantly simplifies the problem. Therefore, a 10-generation PSO optimization is conducted with four particles applied in total. The

initial velocities of these particles are randomly assigned. To increase the convergence rate, the initial locations of the four particles are evenly distributed in the search space. Hence the initial locations of the four particles on duty are given by (-0.15, -0.2); (-0.3, -0.2); (-0.15, -0.5); (-0.3, -0.5)

3.5.3 PSO Coefficients

c_1 and c_2 are acceleration coefficients that separately limit the size of the steps that particles take toward the particle best (p^i) and the group best (p^g), where c_1 = 2, and c_2 = 0.5. The inertial weight *w* is used to control the size of the local searching area of the particle, which is adjusted dynamically as the optimization goes [23].

After each circulation, *w* is reduced for the next turn, following the equation

$$w = w - \left(w \times \frac{N}{10}\right). \quad (16)$$

The beginning value of *w* is set to be 0.5 so that particles can adapt the global search. The particles are then gradually converted from a global search to a local search, with the initial weight *w* being reduced in the conversion.

3.6 Droplet and Micropillar Geometry Constructions

In order to determine the target droplet shape exhibiting these geometric features on a deformed triangular micropillar structure, the open-source software Surface Evolver, developed by Brake, was used to find the equilibrium droplet morphology with different liquid volumes in the absence of any external force and dynamic effects. The surface of the droplet is shaped by the rule of minimizing the free energy, and then it is modified depending on the given geometric constraints from the PSO-generated micropillar shape. The energy applied in this case focuses on surface tension and gravitational energy [34].

Each side of the micropillar shape is defined by a function that correlation from 100 scattered point locations generated from the Bezier curve by conducting a quartic polynomial regression. Three functions serve as the boundary constraints for growing the droplet in Surface Evolver. Some elements should be contained in the definition section, which include declarations, the specific parameters designed according to the model, the necessary defined functions for various forms of energy, and the boundary constraints on the motion of vertices.

The droplet volume is input manually into Surface Evolver to obtain the same solid-liquid interfacial area (i.e., substrate area) $A_{sl} = 7.85 \times 10^{-8}$ m^2, and the same liquid-vapor interfacial area, $A_{lv} = 1.39 \times 10^{-8}$ m^2. The equilibrated droplet shape pinned on the micropillar is then generated by Surface Evolver, and output in .stl format for further operation. To avoid a high aspect ratio mesh which could cause errors in further computation steps, the droplet shape needs to be rebuilt in COMSOL to obtain a more uniform mesh density.

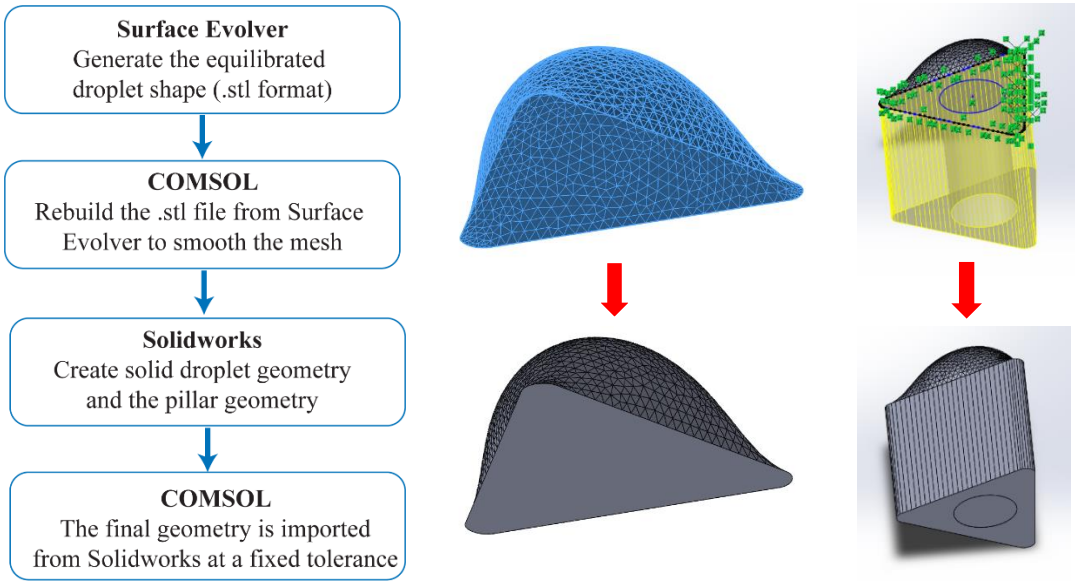

(a) (b) (c)

Figure 8. Optimization of the micropillar shape. (a) Geometry operation flow chart. (b) Create the solid droplet geometry in Solidworks from the shell droplet shape. (c) Create the pillar structure in Solidworks.

Solidworks is applied to build the droplet and micropillar geometries based on the droplet shape obtained from Surface Evolver. The refined droplet shape created by COMSOL is opened by Solidworks and creates the bottom surface of the droplet. The droplet surface and the bottom surface are knitted together to form a solid geometric structure for the droplet. A sketch of the contour of the bottom surface is later generated by manually connecting all the vertices, which is followed by an extrude operation for creating a micropillar geometry of 10 um height. The water inlet is located at the center of the pillar, which is created with a constant pore diameter of 5 um. Finally, the droplet and pillar geometry are imported into COMSOL for the next simulation, with an absolute import tolerance of 1.0×10^{-5}.

3.7 Flow Chart for Optimizing the Micropillar Geometry

Figure 9 shows the general flow chart for micropillar shape optimization. The optimizing process is achieved by using the PSO Algorithm to iteratively search for the best location of the control points. Four particles are assigned as four candidate solutions, which represent four Bezier curves (i.e., micropillar shape) varying with each generation.

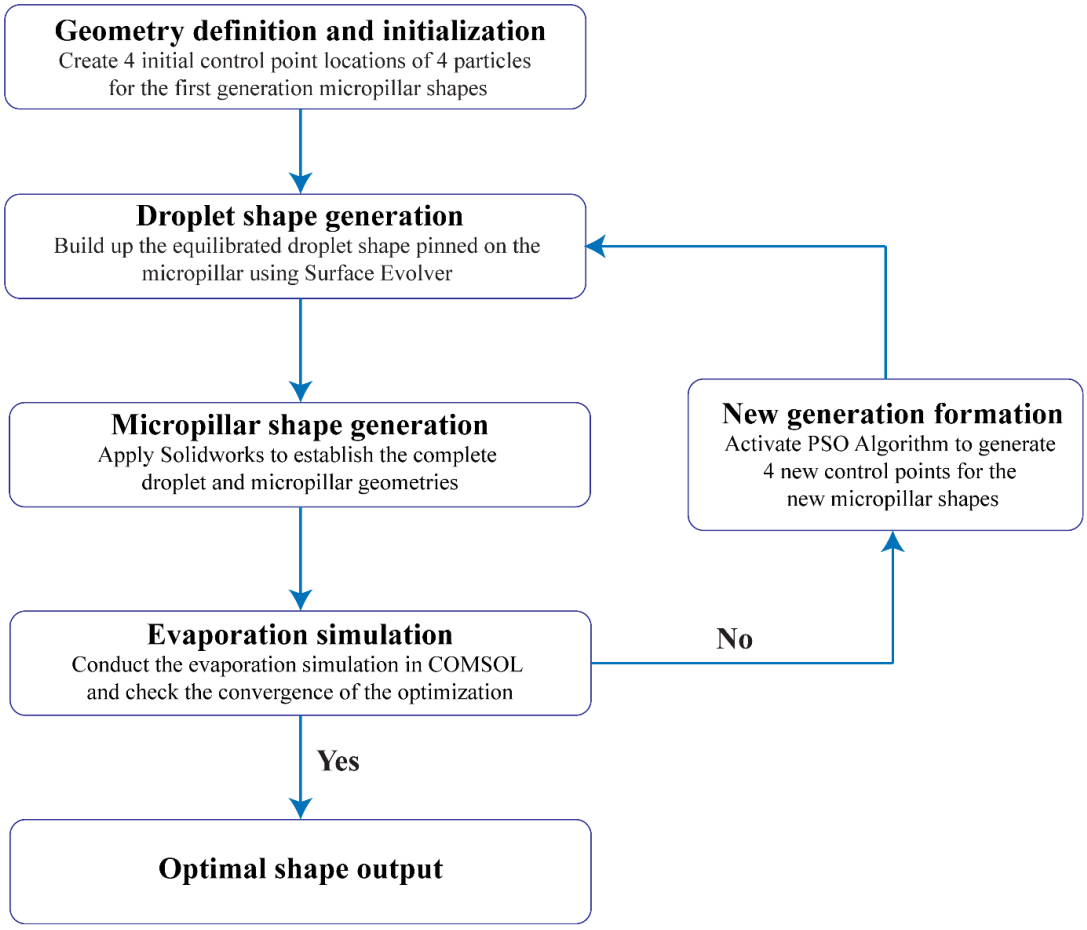

Figure 9. General flow chart for micropillar shape optimization

The equilibrated droplet shapes are generated by Surface Evolver based on the imported pillar shapes. Then, Solidworks is applied to create micropillar geometries based on the geometric operation process introduced in section 4.6. After the micropillar geometries have been built up, the evaporation simulation is conducted in

COMSOL and yields the objective value (i.e., heat transfer coefficient) of the particle. As long as the objective values of all the particles are imported into the PSO algorithm, we are able to go on establishing the micropillar shapes generated in Matlab for the next generation. After several iterations of generations, the shape optimization loop achieves final convergence and outputs the optimal shape.

Chapter 4 Validation to the Reliability of Simulation

To validate the reliability of the simulation method, a set of additional computational simulations with the same simulation method and corresponding evaporative experiments were performed. Both two aspects of the investigation were based on the baseline triangular micropillar structure, and conducted to respectively obtain the heat transfer coefficient and evaporative flux under the substrate temperature with 60°C, 70°C, 80°C, 90°C, and 98°C. In order to investigate the evaporative heat transfer performance experimentally, a single triangular micropillar with two RTD elements was prepared by microfabrication processes, and a customized thermal testing platform which aims at performing the evaporation experiments was designed to form an equilateral triangular droplet on the top of the micropillar. The final validation is achieved by comparing the heat transfer coefficient and evaporative flux from simulation results with that from the experimental measurement.

4.1 Micropillar Fabrication and RTD Calibration

4.1.1 Fabrication Process

To enable the formation of equilibrium asymmetric droplets in evaporation experiment, porous micropillar structure with circular, square and triangular cross sections was microfabricated on a 4" double polished silicon wafer(<1 0 0>, 300 μm thick, University Wafer) with the process of chemical vapor deposition (CVD), photolithography and reactive-ion etching (RIE). The oxide layer (about 450 nm thick) was first grown on both sides of the silicon wafer, which was placed in a tube furnace (Lindberg/Blue M) at 1100 °C for 14 hours. The 125 nm thick platinum resistance temperature detector (RTD) and heater were then deposited on the backside

of the wafer by sputtering (Kurt J. Lesker, PVD 75) and lift-off process. By removing silicon oxide layer with RIE and removing silicon with deep reactive-ion etching (DRIE) on the back side of the wafer, a deep hole was fabricated at the center of the silicon wafer. Fabricating three different shapes of the micropillar structures on the front side followed the same process as fabricating the hole on the backside.

4.1.2 Bonding and Calibration

After removing the chemical residues from the finished micropillar structure samples, two pairs of copper wires were used to connect the RTD and heater with the multimeter and the DC power source respectively. Calibration of the RTD was required before mounting the sample on the thermal test platform. By placing the sample in an oven (Fisher, Isotemp 15-103-0503, USA) and changing the temperature from 30 °C to 100 °C with intervals of 10 °C, the electrical resistances of the RTD in different temperature were recorded by multimeter and used to generate a curve about the relationship between the temperature and the electrical resistance.

4.2 Experimental Methods for Studying Evaporative Heat Transfer Performance

In order to investigate the heat transfer performance of droplet evaporating on the triangular micropillar, the evaporation experiments are performed under steady-state conditions to guarantee that the shape of the droplet was maintained constant by feeding the working fluid to the droplet continuously. Figure 10. shows the schematic of the experimental setup illustrating that a pressure-driven liquid feed system was installed in the experimental platform. The experimental apparatus consisted of three major components: a working liquid delivery system shown in Fig. 10(e), a sample mounting platform shown in Fig. 10(d), and a data acquisition system. Compressed

nitrogen gas originally stored in a nitrogen tank was pumped at a regulated pressure to the reservoir containing working liquid. Thus, the working liquid was immediately pumped from the reservoir to the single micropillar by the steady nitrogen gas flow. The flow rate of the working liquid flowing out of the reservoir was monitored by a microfluidic sensor. The downstream flow pressure was monitored by a pressure sensor. The mass flow rate measured by the flow sensor indicates the evaporation rate of the droplet in the same value since the speed of the water supplying to the droplet is equal to that of the water evaporating from the droplet. A DC power supply as the power source and a multimeter as the temperature sensor, which ware connected with the copper wires, were bonded to the two RTD elements integrated on the backside of the sample. A multimeter was used to measure the electrical resistance in the RTD elements during the experiment. Since the detected electrical resistance is proportional to the local temperature, the substrate temperature of the micropillar could be obtained by monitoring the electrical resistance variation.

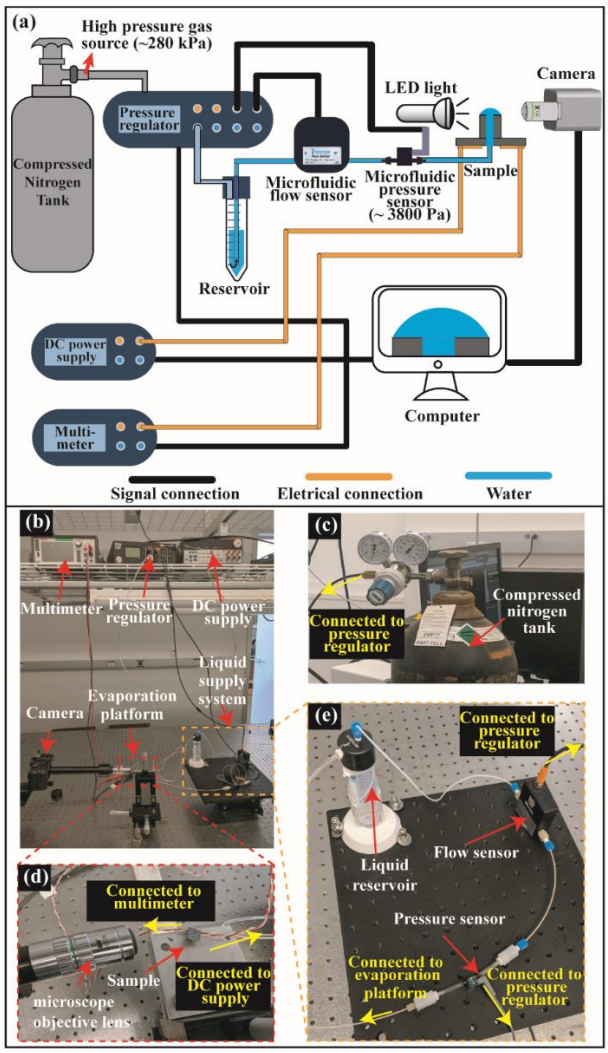

Figure 10. (a) Schematic drawing of the experimental setup. (b)-(e) Photograph of the experimental setup

4.2.1 Preparation of the Desired Droplet at Steady State

Before the evaporation experiment, deionized (DI) water was pumped in a specific pressure to grow a microdroplet with the desired geometry on the triangular micropillar, by which the shape of microdroplet formed in the experiment is exactly same as that generated by the computational modeling.

For modeling the shape of the microdroplet, the open-source software called Surface Evolver was used to automatically generate the geometry when the certain tension,

contact angle, and droplet volume were input. The target droplet shape was controlled to possess the solid-liquid contact perimeter of 314 μm, and liquid-vapor interfacial area of 1200 μm² by adjusting the volume to the desired value.

When it comes to growing a droplet on the micropillar, it was greatly challenging for the pressure regulator to adjust to maintain the droplet in the shape we expect. The pumping pressure was supposed to be cautiously adjusted as the droplets gradually grew on the micropillar until the final droplet with the desired shape had been found. To be specific, when the liquid was first pumped out of the hole of micropillar and formed a small convex meniscus along the center pore, the Laplace pressure was measured to be 3.87 kPa. Because of the viscous pressure loss along with the tubing, a pressure difference between the inner and outer pore occurred to produce a pressure barrier that could prevent further growth of the droplet. After that, with the pumping pressure further increasing, the liquid would quickly wet the complete top surface of the micropillar, which resulted in a drastic increase in the droplet radius with a sharp drop in the Laplace pressure. In this situation, the pumping pressure must be immediately reduced to prevent the droplet bursting. Subsequently, the microdroplet could be effectively controlled to get to the desired shape by manipulating the pressure regulator with certain pumping pressure. When taking the Laplace pressure of the microdroplet into the account, which has a very close relationship with the droplet shape, it is supposed to supply the working liquid with a constant pressure to ensure the droplet to maintain a stable geometry regardless of the evaporation rate since the viscous pressure is significantly smaller than the Laplace pressure.

In order to obtain the microdroplet shape from the experiment, matching with the desired droplet geometry generated by Surface Evolver, it was necessary to slightly change the head pressure of the working fluid by the pressure regulator until the ratio

between the droplet height and the side length measured from the experimental droplet image reached the target value calculated based on the Surface Evolver result. After the measurement, this ratio is equal to 0.46.

4.2.2 Evaporation Heat Transfer Experiments

In the beginning, the opening nitrogen tank released the compressed gas to force the working liquid which is stored in the liquid reservoir. The liquid was pumped into the micropillar structure with the specific pressure regulated by the pressure regulator. After a series of steps, we have discussed above, we were able to obtain the desired droplet geometry. Then, the DC power source was turned on, and the substrate of the micropillar was gradually heated until the temperatures of the substrate reached to the target temperatures (60°C, 70°C, 80°C, 90°C, and 98°C). During the experiment, the substrate temperature was obtained based on the electrical resistance of the RTD elements collected by the multimeter. The evaporation rate of the microdroplet was originated from the flow rate which was collected by the flow rate sensor. Only when the steady-state was confirmed that the variations of the temperature and flow rate were less than 1% over 30 minutes, could the results be recorded.

Chapter 5 Results and Discussion

5.1 Validation Results

Figure 11. shows the comparison between experimental and numerical values of total evaporative flux and heat transfer co-efficient for an evaporating droplet confined on an equilateral triangular micropillar. The substrate is heated to temperatures ranging from 60°-98° C. The evaporative flux is calculated as the total evaporation rate per unit solid liquid interfacial area using the following equation:

$$J = \frac{m_v}{A_{sl}} \tag{17}$$

Here, m_v is the total evaporation rate, A_{sl} is the solid-liquid interfacial area, where the evaporation rate is equal to the mass flow rate measured by the mass flow sensor. Heat transfer co-efficient, h was calculated using the following equation:

$$\text{h}=\frac{m_v h_{fg}}{A_{sl}(T_{lv} - T_\infty)} \tag{18}$$

where T_{lv} is the liquid-vapor interfacial temperature, and T_∞ is the ambient temperature. The latent heat of vaporization, h_{fg}, was determined by the corresponding substrate temperature, T_{sub}.

Evaporative flux increases more sharply at higher temperatures (>80°C) since saturated vapor concentration at liquid-vapor interfacial temperature T_{lv} increases at a faster rate. This nonlinear increase rate is due to the nonlinear relationship between the equilibrium pressure and the liquid-vapor interfacial temperature [35]. As a result, vapor diffusion around the droplet meniscus is enhanced due to the higher concentration gradient. The heat transfer co-efficient follows the same trend. As the substrate temperature is increased from 60 °C to 98° C, the heat transfer co-efficient is increased by 152%.

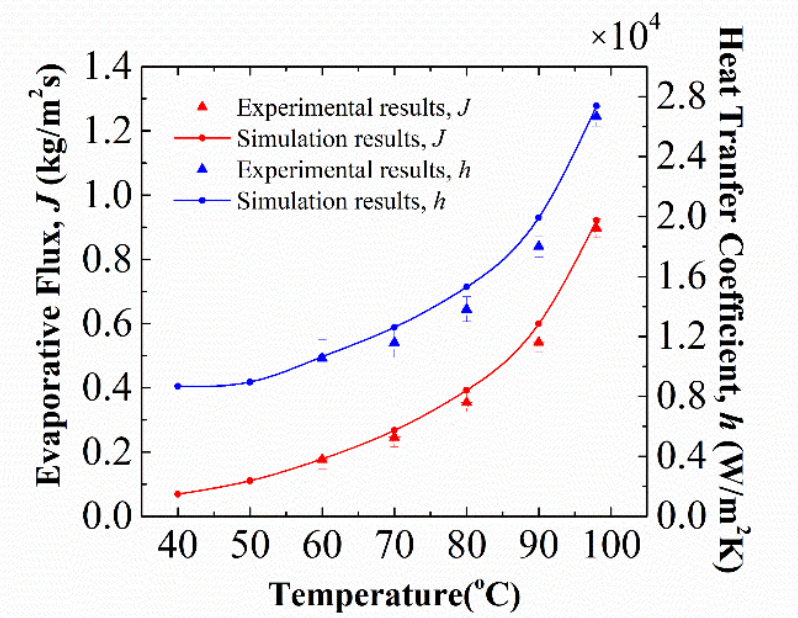

Figure 11. Evaporative flux and the heat transfer coefficient obtained form simulation results and experimental measurement for microdroplets evaporating on an equilateral triangular micropillar.

Evaporative flux and heat transfer co-efficient from experiment and simulation agree reasonably with each other. The relative errors between the two approaches range from 1% to 10%. The discrepancy in results can be attributed to some of the assumptions made in the simulation. For example, in the simulation, the conduction resistance through the substrate has been neglected. Moreover, the temperature measured by the RTD sensor is slightly different than the actual substrate temperature. So, in the simulation, the temperature at the substrate as well at the liquid-vapor interface is overpredicted by 6% which causes about 20% more diffusion. [35]

5.2 Optimized Micropillar Shape by PSO

The PSO algorithm is calculated until the convergence is reached. Here, convergence is characterized by gradually decreasing variance as discussed in section 3.5.1. As

shown in Fig. 10 (a), with each generation, the variance gets smaller and becomes as small as 0.01645 in the 9th generation, which demonstrates the achievement of convergence. Figure 10(b) provides the convergence history of particle locations. Starting from the evenly distributed particle locations at generation 1, the four particles gradually move to the upper left region. In generation 9, all the particles converge around the group best particle, showing the convergence of the optimization process.

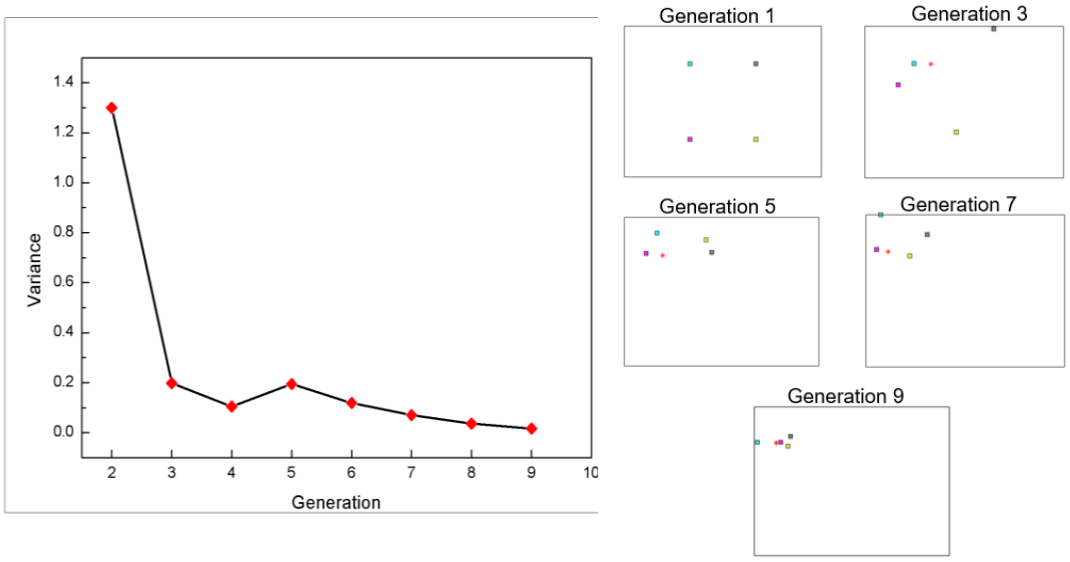

(a) (b)

Figure 10 (a) variance of temperatue changes with the growth of generation. (b) Control point locations in different generations.

The baseline triangular micropillar shape and the optimized micropillar shape are shown in Figure 11. Compared with the equilateral triangular shape, the optimized shape is a curved concave triangular shape. The control point location for the optimized shape is located at (-0.399, -0.196).

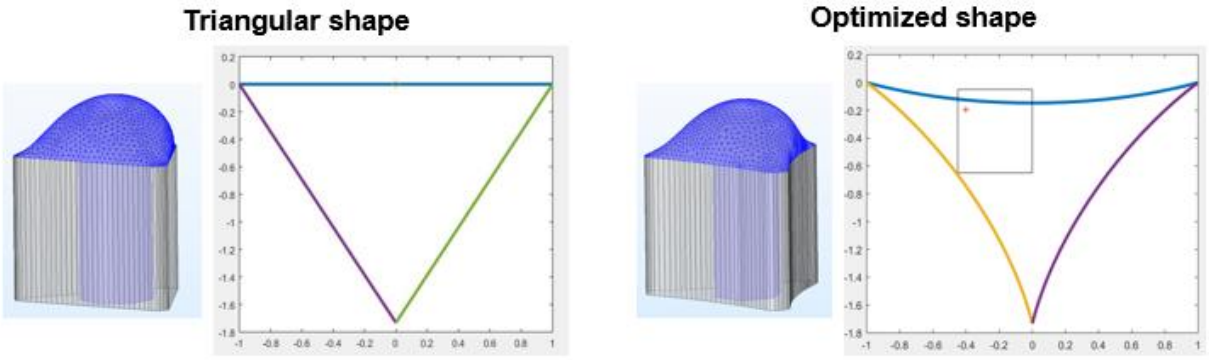

Figure 11. (a) Baseline triangular micropillar shape and geometry. (b) Optimized concave triangular micropillar shape and geomerty

5.3 Heat Transfer Enhancement with the Optimized Micropillar Shape

Figure 12 shows the objective value (i.e., heat transfer coefficient) of the group best particle at different generations. The heat transfer coefficient of the group best particle becomes constant after generation 5 and corresponds to the optimized micro-pillar shape.

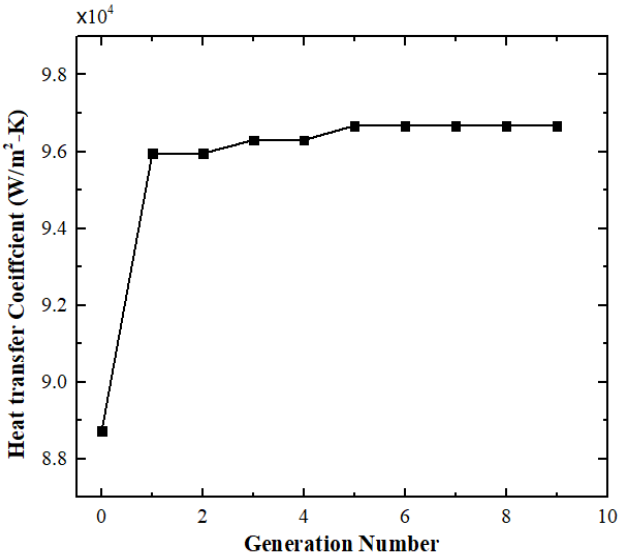

Figure 12. Heat transfer co-efficient, h of the group best particle at each generation. The objective value becomes constant after 5th generation.

The heat transfer coefficient is improved from a baseline value of 8.87×10^4 W/m^2-K to 9.67×10^4 W/m^2-K, which is a 9% enhancement.

5.4 Variation of Two Droplet Characteristics

As reported earlier, the difference in the heat transfer coefficient is resulted by the varied meniscus shape. For an evaporating droplet, the maximum evaporation rate is observed at the contact line region since the thickness of the liquid layer in the vicinity of the contact line is very small compared to the bulk of the liquid and has a very smaller conduction resistance across the liquid film. Practically, by increasing the contact line length, the total evaporation rate can be enhanced. This was demonstrated by changing the droplet shape from spherical to an asymmetric shape by using a triangular micropillar, where the perimeter-to-wetted area ratio has been increased. This change in the droplet shape also resulted in larger meniscus curvature which contributes to a higher vapor diffusion rate. As a result, both mass and energy transfer rate have been enhanced. For our current study, the comparative improvement in the contact line length and the meniscus curvature is shown in table 3. Compared to the droplet confined on the equilateral triangle shape micropillar, the subsequent droplets confined on the micropillar with concave edges have increased perimeter-to-wetted area ratio with each generation. Finally, the optimized shape (at generation 5 and 6) has as high as 5.121 % increment. Additionally, increasing curvature of the droplet meniscus is noted with each generation and the droplet with the optimum shape has a 2.57% higher curvature than the reference droplet. Combined together, the increase in curvature and perimeter-to-area ratio causes 9% increase in the heat transfer coefficient for the optimized droplet.

Table 3.

Comparison of meniscus curvature and perimeter-to-wetted area ratio of group best particle at each generation

Generation number	% increase in contact line length (mm)/Wetted area (mm^2)	% increase in curvature (1/m)
1-2	4.614563884	1.09
3-4	5.681515071	1.1
5-6	5.121365698	2.57

5.5 Analysis to theTemperature and Concentration Contour

Temperature distribution in the solid and liquid domains are shown in Figure 13. for the baseline shape (Fig. 13(a)) and optimum shape (Fig. 13(b)). For each microdroplet shape, the maximum temperature is observed at the contact line, where the thickness of local liquid film and the conduction resistance are minimum.

Conversely, the minimum temperature is observed at the top most point on the droplet meniscus, where the liquid has the highest thickness and maximum conduction resistance. Compared with baseline shape, the temperature at the contact line is also smaller in case of optimized shape since evaporative flux is more, which causes more heat to dissipate from the micropillar surface.

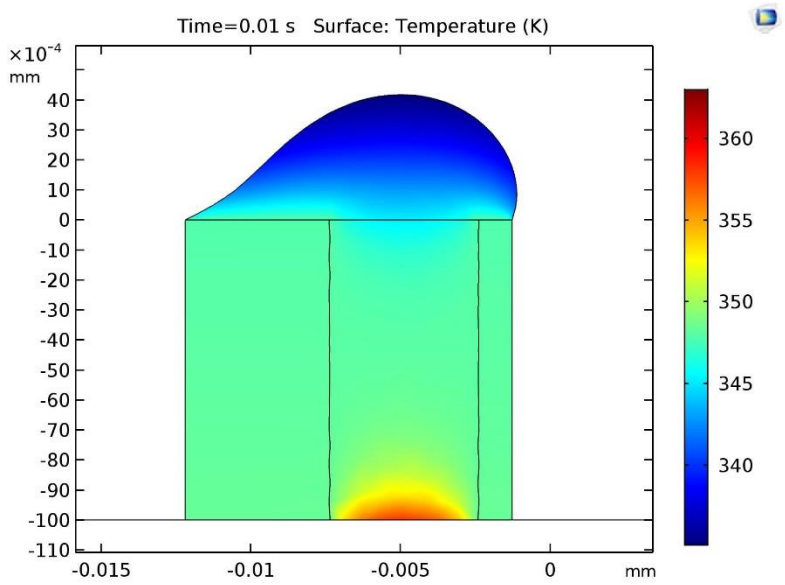

(a)

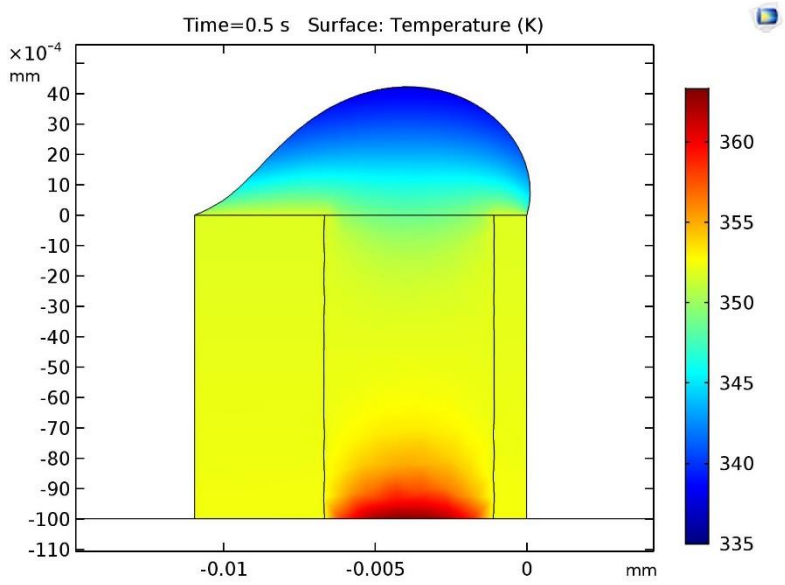

(b)

Figure 13. Temperature contour for baseline shape(a) and optimum shape(b)

Fig. 14(a and b) shows the vapor concentration for the two cases. Since the contact line region has the maximum interfacial temperature, vapor concentration observed along the line is also higher, which leads to a higher evaporation rate. Also, the optimized shape has higher curvature. The difference in curvature between baseline shape and optimum shape is hardly observed because the measurement of the droplet

curvature shows only a 2.57% increase. However, this increment results in more densely distributed concentration gradients around the solid-vapor-liquid contact line, which is more enhanced near the corners of the micropillar. This leads to more vapor diffusion and eventually more evaporation from the droplet meniscus.

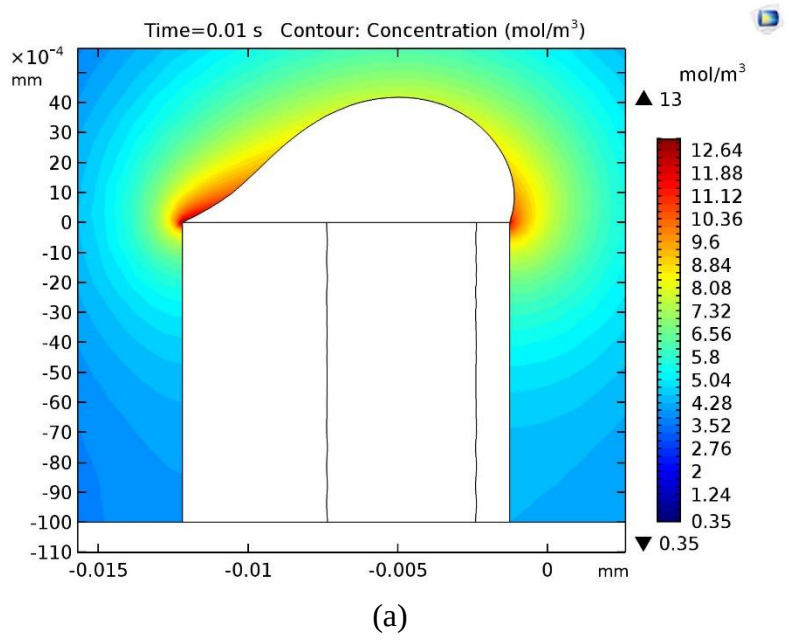

(a)

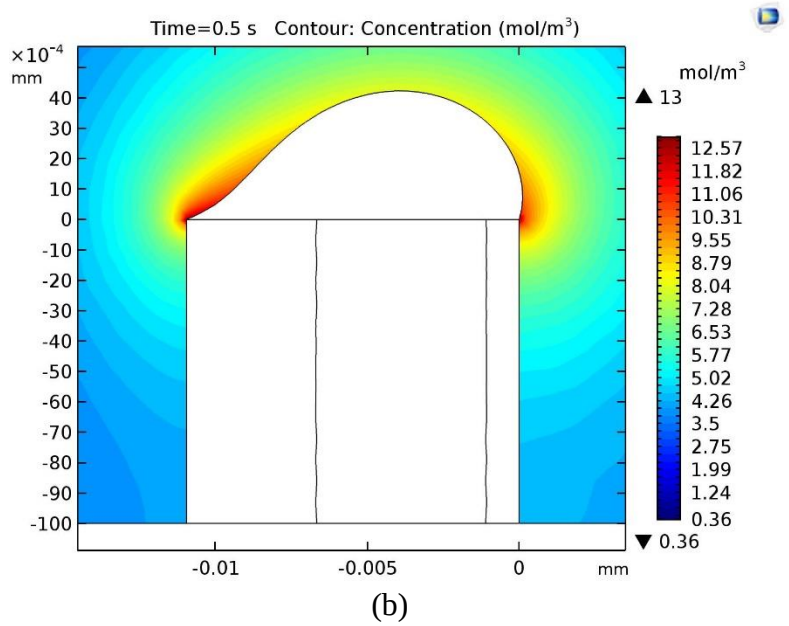

(b)

Figure 14. concentration contour for baseline shape(a) and optimum shape(b)

Chapter 6 Conclusion

In this thesis, two factors are investigated to perform the shape effect of droplet evaporation on a micropillar. Based on the Particle Swarm Optimization algorithm, the shape optimization loop is developed to trace the desired droplet shape with highest evaporation rate and desired micropillar shape with maximum heat transfer coefficient. The shape optimization method integrates shape generation by Matlab, equilibrated droplet shape generation by Surface evolver, and evaporation simulation by COMSOL into an iteration loop. The thermal-diffusion model is developed in COMSOL to predict thermal transport in droplet evaporation. The shape generation is controlled by the PSO algorithm to update the geometries into new iterations based on the objective value. The optimum shape is output with a 9% improvement in heat transfer coefficient when convergence criterion reaches after 9 iterations. By comparison between experimental and numerical values of total evaporative flux and heat transfer coefficient for an evaporating droplet confined on an equilateral triangular micropillar, it could be confirmed that simulation results agree well with the experimental measurement with the relative error ranging from 1% to 10%.

Reference

[1] E. Beyne, "The rise of the 3rd dimension for system intergration," in *2006 International Interconnect Technology Conference*, 2006: IEEE, pp. 1-5.

[2] S. Cheramy *et al.*, "3D integration process flow for set-top box application: description of technology and electrical results," in *2009 European Microelectronics and Packaging Conference*, 2009: IEEE, pp. 1-6.

[3] V. K. Pamula and K. Chakrabarty, "Cooling of integrated circuits using droplet-based microfluidics," in *Proceedings of the 13th ACM Great Lakes symposium on VLSI*, 2003: ACM, pp. 84-87.

[4] M. Mochizuki, Y. Saito, F. Kiyooka, and T. Nguyen, "The way we were and are going on cooling high power processors in the industries," *FUJIKURA TECHNICAL REVIEW*, vol. 36, p. 53, 2007.

[5] A. Bar-Cohen[1], J. J. Maurer, and J. G. Felbinger, "DARPA's intra/interchip enhanced cooling (ICECool) program," in *CS MANTECH Conference, May 13th-16th*, 2013.

[6] B. Agostini, M. Fabbri, J. E. Park, L. Wojtan, J. R. Thome, and B. Michel, "State of the art of high heat flux cooling technologies," *Heat Transfer Engineering*, vol. 28, no. 4, pp. 258-281, 2007.

[7] S. Wang, Y. Yin, C. Hu, and P. Rezai, "3D integrated circuit cooling with microfluidics," *Micromachines*, vol. 9, no. 6, p. 287, 2018.

[8] D. B. Tuckerman and R. F. W. Pease, "High-performance heat sinking for VLSI," *IEEE Electron device letters*, vol. 2, no. 5, pp. 126-129, 1981.

[9] R. Mandel, A. Shooshtari, and M. Ohadi, "Thin-film evaporation on microgrooved heatsinks," *Numerical Heat Transfer, Part A: Applications*, vol. 71, no. 2, pp. 111-127, 2017.

[10] R. Ranjan, J. Y. Murthy, and S. V. Garimella, "Analysis of the wicking and thin-film evaporation characteristics of microstructures," *Journal of Heat Transfer*, vol. 131, no. 10, p. 101001, 2009.

[11] R. Ranjan, J. Y. Murthy, and S. V. Garimella, "A microscale model for thin-film evaporation in capillary wick structures," *International Journal of Heat and Mass Transfer*, vol. 54, no. 1-3, pp. 169-179, 2011, doi: 10.1016/j.ijheatmasstransfer.2010.09.037.

[12] H. Wang, S. V. Garimella, and J. Y. Murthy, "Characteristics of an evaporating thin film in a microchannel," *international journal of heat and mass transfer*, vol. 50, no. 19-20, pp. 3933-3942, 2007.

[13] M. Hanlon and H. Ma, "Evaporation heat transfer in sintered porous media," in *8th AIAA/ASME Joint Thermophysics and Heat Transfer Conference*, 2003, p. 3092.

[14] H. Ma, P. Cheng, B. Borgmeyer, and Y. Wang, "Fluid flow and heat transfer in the evaporating thin film region," *Microfluidics and Nanofluidics*, vol. 4, no. 3, pp. 237-243, 2008.

[15] Z. Lu, K. L. Wilke, D. J. Preston, I. Kinefuchi, E. Chang-Davidson, and E. N. Wang, "An ultrathin nanoporous membrane evaporator," *Nano letters*, vol. 17, no. 10, pp. 6217-6220, 2017.

[16] L. Dong, X. Quan, and P. Cheng, "An experimental investigation of enhanced pool boiling heat transfer from surfaces with micro/nano-structures," *International Journal of Heat and Mass Transfer*, vol. 71, pp. 189-196, 2014.

[17] W. Qu and I. Mudawar, "Experimental and numerical study of pressure drop and heat transfer in a single-phase micro-channel heat sink," *International Journal of Heat and Mass Transfer*, vol. 45, no. 12, pp. 2549-2565, 2002.

[18] W. Qu and I. Mudawar, "Flow boiling heat transfer in two-phase micro-channel heat sinks—I. Experimental investigation and assessment of correlation methods," *International journal of heat and mass transfer*, vol. 46, no. 15, pp. 2755-2771, 2003.

[19] S. Shuai, Z. Du, B. Ma, L. Shan, B. Dogruoz, and D. Agonafer, "Numerical Investigation of Shape Effect on Microdroplet Evaporation," in *ASME 2018 International Technical Conference and Exhibition on Packaging and Integration of Electronic and Photonic Microsystems*, 2018: American Society of Mechanical Engineers, pp. V001T04A010-V001T04A010.

[20] A. R. Yıldız, "A novel particle swarm optimization approach for product design and manufacturing," *The International Journal of Advanced Manufacturing Technology*, vol. 40, no. 5-6, p. 617, 2009.

[21] N. Lyu and K. Saitou, "Topology optimization of multicomponent beam structure via decomposition-based assembly synthesis," *Journal of Mechanical Design*, vol. 127, no. 2, pp. 170-183, 2005.

[22] R. Eberhart and J. Kennedy, "A new optimizer using particle swarm theory," in *MHS'95. Proceedings of the Sixth International Symposium on Micro Machine and Human Science*, 1995: Ieee, pp. 39-43.

[23] P. Fourie and A. A. Groenwold, "The particle swarm optimization algorithm in size and shape optimization," *Structural and Multidisciplinary Optimization*, vol. 23, no. 4, pp. 259-267, 2002.

[24] U. K. Wickramasinghe, R. Carrese, and X. Li, "Designing airfoils using a reference point based evolutionary many-objective particle swarm optimization algorithm," in *IEEE Congress on Evolutionary Computation*, 2010: IEEE, pp. 1-8.

[25] H. Hu and R. G. Larson, "Analysis of the effects of Marangoni stresses on the microflow in an evaporating sessile droplet," *Langmuir*, vol. 21, no. 9, pp. 3972-3980, 2005.

[26] H. Hu and R. G. Larson, "Marangoni effect reverses coffee-ring depositions," *The Journal of Physical Chemistry B*, vol. 110, no. 14, pp. 7090-7094, 2006.

[27] F. Girard, M. Antoni, and K. Sefiane, "On the effect of Marangoni flow on evaporation rates of heated water drops," *Langmuir*, vol. 24, no. 17, pp. 9207-9210, 2008.

[28] S. Semenov, V. M. Starov, R. G. Rubio, and M. G. Velarde, "Computer simulations of evaporation of pinned sessile droplets: influence of kinetic effects," *Langmuir*, vol. 28, no. 43, pp. 15203-15211, 2012.

[29] Y. A. Cengel and M. A. Boles, "Thermodynamics: an engineering approach," *Sea*, vol. 1000, p. 8862, 2002.

[30] Y. Shi, "Particle swarm optimization: developments, applications and resources," in *Proceedings of the 2001 congress on evolutionary computation (IEEE Cat. No. 01TH8546)*, 2001, vol. 1: IEEE, pp. 81-86.

[31] J. Li, T. Wray, and R. K. Agarwal, "Shape optimization of supersonic bodies to reduce sonic boom signature," in *34th AIAA Applied Aerodynamics Conference*, 2016, p. 3432.

[32] M. E. Mortenson, *Mathematics for computer graphics applications*. Industrial Press Inc., 1999.

[33] R. Winkel, "Generalized Bernstein polynomials and Bézier curves: An application of umbral calculus to computer aided geometric design," *Advances in Applied Mathematics*, vol. 27, no. 1, pp. 51-81, 2001.

[34] K. A. Brakke, "The surface evolver," *Experimental mathematics*," vol. 1, no. 2, pp. 141-165, 1992.

[35] Li Shan, Junhui Li, and Binjian Ma, "Experimental investigation of evaporation from asymmetric microdroplets confined on heated micropillar structures", Experimental Thermal and Fluid Science, vol. 109, 2019.